Encapsulating Metal Nanoparticles into a Layered Zeolite Precursor with Surface Silanol Nests Enhances Sintering Resistance

Ang Li,[1] Yuyan Zhang,[1] Christopher J. Heard,[1] Kinga Gołąbek,[1] Xiaohui Ju,[2] Jiří Čejka,[1] and Michal Mazur*[1]

1Department of Physical and Macromolecular Chemistry, Charles University, Hlavova 8, 128 43 Prague 2, Czech Republic, corresponding author: michal.mazur@natur.cuni.cz

2Department of Surface and Plasma Science, Faculty of Mathematics and Physics, Charles University, V Holešovičkách 2, 18000, Prague 8, Czech Republic

Abstract

Supported metal nanoparticles are widely used as heterogeneous catalysts but often deactivated due to sintering under harsh conditions, especially at high temperatures. Sintering can be prevented by confining metal species into a porous matrix, although supports rarely provide additional stabilization effects. Herein, we used silanol-rich layered zeolite, IPC-1P, to stabilize ultra-small Rh nanoparticles. By adjusting the interlayer space of the precursor through swelling, we prepared various architectures, including microporous Rh@IPC-4_C12 and disordered mesoporous Rh@IPC_C22. By in-situ scanning transmission electron microscopy, we confirmed that immobilized Rh nanoparticles are resistant to sintering at high temperatures (650 °C for 2hrs). Our density functional theory (DFT) calculations indicated that small Rh clusters strongly bind to the surface silanol quadruplets at IPC-1P layers through hydrogen transfer to the metallic particles, while high silanol density hinders migration on the surface. Ultimately, combining swelling with long-chain surfactant and utilizing metal-silanol interactions resulted in a novel, catalytically active zeolitic material termed Rh@IPC_C22.

Keywords:

zeolites • mesoporous materials • rhodium • metal-support interaction • layered materials

Table of Content
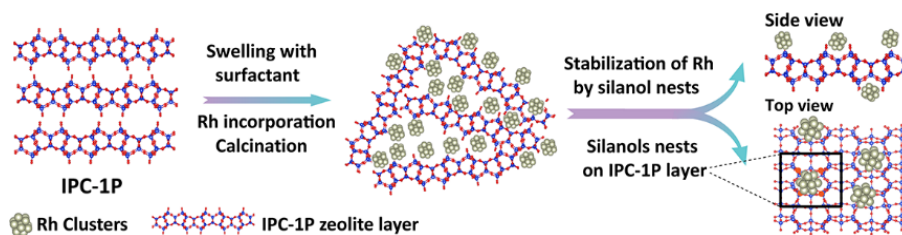
IPC-1P, a layered zeolite precursor with a relatively high density of surface silanols can be swollen using docosyltrimethylammonium hydroxide and simultaneously functionalized with ultra-small Rh nanoparticles. The resulting mesoporous zeolitic material Rh@IPC_C22 has a high layer disordering without microporosity. In-situ heating STEM imaging and DFT simulations show that metal-silanol interactions strongly stabilize Rh nanoparticles against thermal sintering.

Highlights:

➢ Sintering-resistant ultra-small Rh nanoparticles were incorporated into the layered zeolite precursor IPC-1P

➢ Various tunable architectures, including microporous Rh@IPC-4_C12 and delaminated mesoporous Rh@IPC_C22, were prepared by adjusting the interlayer molecule size

➢ Nanoparticle evolution and changes in material architecture were tracked by in-situ heating STEM

➢ Mesoporous Rh@IPC_C22 is a suitable model for studying metal-zeolite interactions thanks to its defined silanol nests and lack of micropore confinement effects

Introduction

Supported metal nanoparticles (MNPs) are effective heterogeneous catalysts in many chemical processes, such as aerobic oxidation, hydrogenation and dehydrogenation, reforming, and water-gas shift reactions.[1] However, these catalysts are deactivated due to leaching or sintering under harsh conditions.[2] The most promising strategy for avoiding MNPs aggregation and further deactivation is to confine highly active metal species into porous matrices, such as metal-organic frameworks, polymers, carbon materials, metal oxides or zeolites.[3] Among these porous supports,

zeolites have several appropriate features for encapsulation, including rigid frameworks, physical and chemical stability, high surface areas, ordered microporous channels, and tunable acid sites.[4] As such, zeolites are ideal supports, with a high degree of tunability.

Various metal encapsulation methods, such as ion-exchange, impregnation, protective organic ligand coordination, and seed-directed transformation have been developed.[6] The main challenges of an efficient metal@zeolite preparation lie in stabilizing metal precursors under synthesis conditions and avoiding their agglomeration.[7] Recently, subnanometric Pt clusters were encapsulated into **MWW** zeolite during the transformation of a swollen 2D zeolite layer precursor into 3D zeolites, showing notable stability against agglomeration (Pt clusters still below 2 nm after 4 cycles of oxidation-reduction treatments at 650 °C), albeit significant loss of metal (~70%).[8] Further studies have indicated that the size of the resulting MNPs can be tuned by adjusting the size of the surfactant used for swelling.[9] This strategy also works in the Assembly-Disassembly-Organization-Reassembly (ADOR) synthesis approach through 3D-2D-3D zeolite layer transformation[10], with two key advantages. On the one hand, post-synthesis modifications avoid harsh hydrothermal conditions. On the other hand, 2D zeolite layers have a defined structure, hence enabling a precise design of daughter zeolites.[11]

ADOR is based on topotactical layer transformation. This method exploits the chemical weakness of the original material (germanosilicate) to separate its constituent layers and form a 2D precursor.[12] The first ADOR parent zeolite was **UTL**. Because **UTL** consists of dense 2D silica layers connected by double-four-ring (D4R) building units,[13] preferentially occupied with Ge atoms,[14] its 3D framework can be hydrolyzed into a 2D layered zeolite precursor (IPC-1P) by removing germanium. The degradation of D4Rs leads to the formation of four silanols (quadruplet silanol nests) on the IPC-1P layer surface. The resulting 0.95-nm-thick layers have a relatively high silanol density (1 silanol per 43 $Å^2$) and are kept together through hydrogen bonding between surface silanols. Nevertheless, the interlamellar space of IPC-1P can be expanded by swelling with long-chain surfactants. During swelling, a metal source can be introduced between IPC-1P layers, as shown by the encapsulation of platinum nanoparticles into ADOR zeolites, i.e., Pt@IPC-2 and Pt@IPC-4. [15]

Research on interactions between metal nanoparticles and zeolites reported thus far has considered two main factors, namely the steric hindrance of metal nanoparticles in micropores and metal-silanol interactions, which are usually challenging to asses.[16] Combining density functional theory (DFT) calculations with integrated differential phase contrast scanning transmission electron microscopy (iDPC-STEM) imaging, Liu et al. evaluated local metal-zeolite strain in a zeolite framework by studying isolated iridium atoms and clusters in **MWW** zeolite (Ir@MWW).[17] Notwithstanding their efforts, it is still challenging to precisely define the metal-silanols interactions and the steric hindrance effects of nanoparticles confined in micropores. Therefore, further research combining experimental data with theoretical calculations should be conducted to describe metal-silanol interactions in zeolites.
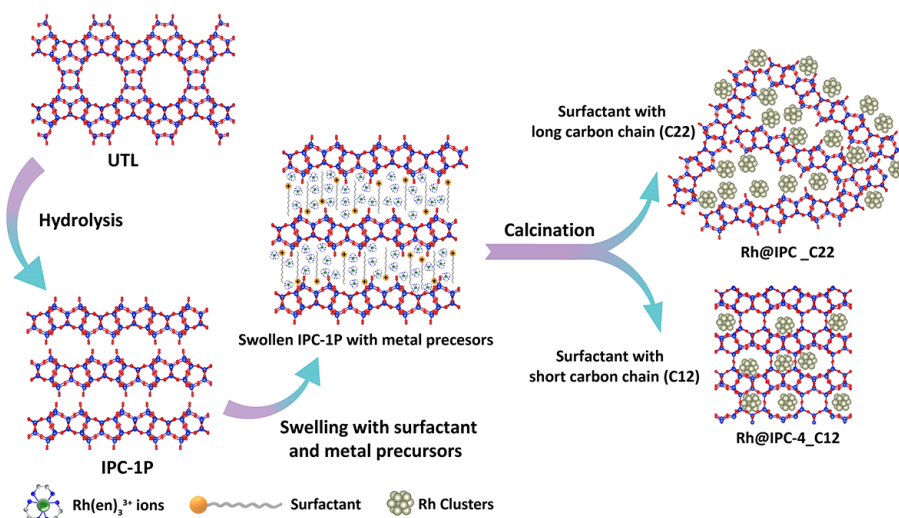
Scheme 1. Synthesis procedure of Rh@IPC materials with different architectures.

In this study, we report the synthesis of a set of rhodium-doped materials (Rh@IPCs) with a tunable architecture prepared from a layered zeolite precursor (IPC-1P), in turn derived from **UTL** germanosilicate (**Scheme 1**). For this purpose, we encapsulated rhodium nanoparticles when swelling IPC-1P with surfactants of various lengths. During swelling and subsequent calcination, we investigated structural changes of these materials. Since in-situ STEM imaging allow us to track the same crystals during thermal treatment, we used this method to analyze the evolution and thermal stability of Rh nanoparticles, thereby gaining insights into the size and distribution of metal species and into interactions between metal species and surface silanols. IPC-1P is an

appropriate candidate for studying metal-silanol interactions given its ordered surface silanols in the form of quadruplet silanol nests. By contrast, single layers of IPC-1P do not have intralayer micropores, ruling out micropore steric hindrance effects on the formation and stability of rhodium nanoparticles. Our experimental approach was supported by DFT calculations, furthering our understanding of the influence of surface silanol nests on the stabilization of metal species and of nanoparticles on layer connectivity/ disordering in final IPC materials.

Results and discussion

Surfactants with hydrophobic carbon chains of various lengths (dodecyltrimethylammonium hydroxide – $C_{12}OH$, cetyltrimethylammonium hydroxide – $C_{16}OH$, and docosyltrimethylammonium hydroxide – $C_{22}OH$) were used to prepare materials denoted as Rh@IPC-4_C12, Rh@IPC_C16, and Rh@IPC_C22, respectively. Their structures were analyzed by powder X-ray diffraction (PXRD). Tracking the position of dominant (002) interlayer peak (**Fig. 1a, c**), we followed changes in the layer spacing of these materials. The PXRD pattern of **UTL** zeolite showed an interlayer peak at 6.2 °2θ, which corresponds to an interlayer d-spacing of 1.42 nm. Acid hydrolysis removed Ge from the **UTL** structure, producing a layered precursor IPC-1P, as confirmed by the shift of the interlayer peak to 8.3 °2θ (d-spacing of 1.06 nm). IPC-1P swelling at an alkaline pH with surfactant molecules of various lengths ($C_{12}OH$, $C_{16}OH$, and $C_{22}OH$) increased the interlayer space, as indicated by the shift of the interlayer diffraction peak towards lower °2θ angles (**Fig. S1**).

The interlayer distance of swollen samples affected the ordering of the layers, and thus interlayer porosity, in the calcined, final material, as shown by the decrease in the dominant peak intensity with the increase of the surfactant length. Using a shorter-chain surfactant ($C_{12}OH$) led to relatively small interlayer distances. Accordingly, during calcination, surface silanols can form oxygen bridges (Si-O-Si) between consecutive layers, yielding IPC-4 (**PCR**) zeolite, with 0.9 nm d-spacing.[10c]

Increasing the length of the surfactant increased the disorder of the layers, as shown by the significant decrease in the intensity of the dominant interlayer peak. When further increasing the surfactant length to $C_{22}OH$, the interlayer peak disappeared after calcination, implying the

formation of a highly disordered structure, albeit with preserved layers, as indicated by the comparison of the simulated PXRD pattern of the IPC-1P monolayer with that of Rh@IPC_C22. The latter showed intralayer peaks without the interlayer dominant peak, in line with SEM imaging.

IPC-1P preserved the morphology of the parent **UTL** (**Fig. S2**) due to hydrogen bonding between surface silanols. Increasing the surfactant length weakened the hydrogen bonding, noticeably changing the crystal morphology. Plate-like crystals were not preserved in Rh@IPC_C22 (**Fig. S2e&f**), which did not contain Rh or Rh_2O_3 particles, as confirmed by lack of peaks around 41.1 °2θ in PXRD patterns.[18]
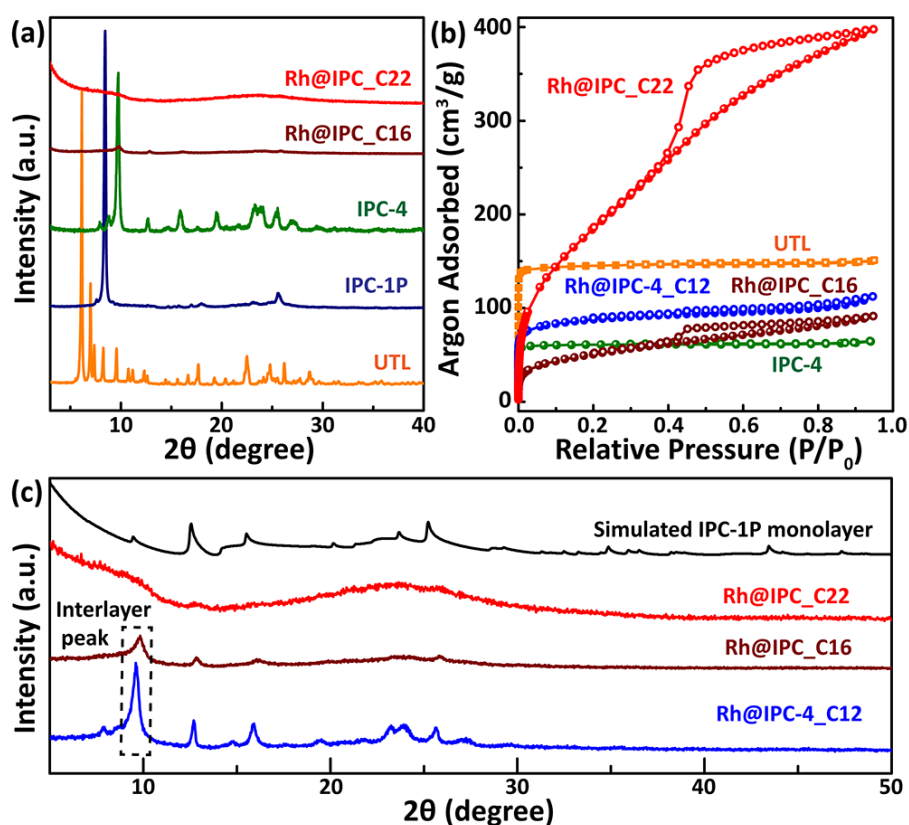

Figure 1. (a) PXRD patterns and (b) argon adsorption–desorption isotherms of UTL, IPC-1P, IPC-4, Rh@IPC zeolitic materials; (c) enlarged PXRD patterns of Rh@IPC-4_C12, Rh@IPC_C16 and Rh@IPC_C22, and simulated PXRD pattern of monolayer IPC-1P.

The textural parameters of the materials were calculated based on argon sorption isotherms (**Table 1** and **Fig. 1b**). Rh@IPC-4_C12 had a higher BET area than standard IPC-4 (236 and 198

m^2/g, respectively) due to incomplete layer connections caused by Rh nanoparticles in interlayer spaces. Rh@IPC_C16 had 162 m^2/g S_{BET}, 122 m^2/g $S_{mes+ext}$, 0.01 cm³/g V_{mic} and 0.12 cm³/g V_{tot}. The significantly lower microporosity indicates that the layers were disordered in the final material. This effect was even more visible in the material swollen with the longest carbon chain molecule (C$_{22}$OH). The resulting Rh@IPC_C22 had 626 m^2/g S_{bet}, and 0.51 cm³/g V_{tot}. In contrast to Rh@IPC-4_C12, the textural parameters of Rh@IPC_C22 were mainly attributed to sorption in mesopores and at the external surface, demonstrating that the layers were not connected orderly. The micropore volume was negligible in comparison with that of the parent **UTL** and daughter IPC-4 zeolites. These findings support our conclusion based on the analysis of PXRD patterns.

The increase in the S_{BET} and V_{tot} parameters, as well as the shape of the Rh@IPC_C22 adsorption-desorption isotherm (showing significant H$_2$ hysteresis), suggests that its layers are mostly disordered and that the interlayer voids are of mesopore size. Conversely, the other IPC materials showed a higher layer ordering, indicating microporosity. For comparison, we prepared a material without Rh particles, denoted as IPC_22. Its structure and texture analysis are shown (**Fig. S3-S5**) and discussed in SI.

Table 1. Textural parameters of UTL, IPC-4, and Rh-incorporated IPC zeolitic materials[a]

Material	S_{BET} [m^2/g]	$S_{mes+ext}$ [b] [m^2/g]	V_{mic} [cm^3/g]	V_{tot} [cm^3/g]	d_1 [c] [nm]	d_2 [d] [nm]
UTL	492	25	0.21	0.25	-	1.42
IPC-4	198	7	0.09	0.10	-	0.91
Rh@IPC-4_C12	236	24	0.09	0.13	2.6	0.91
Rh@IPC_C16	162	72	0.04	0.12	3.3	0.91
Rh@IPC_C22	626	540	0.02	0.51	4.0	-

[a] Supplementary note in SI; [b] Sum of mesopores area and external surface area ($S_{mes+ext}$) was calculated by t-plot method; [c] d-spacing of a swollen precursor; [d] d-spacing of the final material

The annular dark field scanning transmission microscopy (ADF-STEM) images shown in **Fig.2a-c** reveal the architectures of Rh@IPC-4_C12, Rh@IPC_C16, and Rh@IPC_C22. In Rh@IPC-4_C12, the IPC zeolite layers were relatively well ordered, most of which connected by oxygen bridges. However, some bonds were disturbed by the Rh nanoparticles. These nanoparticles, with an average size of 1.83 nm, were uniformly distributed in the material and mostly located between layers (**Fig. 2a**). The Rh nanoparticles acted as "pillars", preventing a full connection of the layers into uniform 3D crystals, in line with textural data.
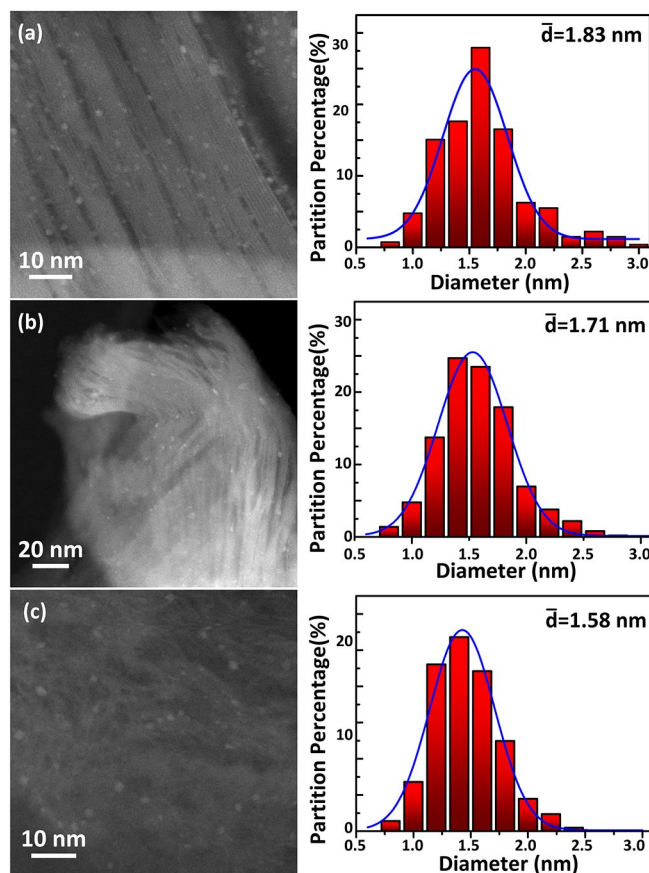

Figure 2. STEM images and corresponding Rh particles size distribution histograms of Rh@IPC-4_C12 (c), Rh@IPC_C16 (d), and Rh@IPC_C22 (e). Average nanoparticle diameters were evaluated using Sauter mean diameter $d_{TEM} = \Sigma n_i d_i^3 / \Sigma n_i d_i^2$.

The IPC-1P zeolite layers in Rh@IPC_C16 (**Fig. 2b**) were less ordered than in Rh@IPC_C12, but they were still connected by oxygen bridges in some parts of the crystals. This architecture derived from the molecular length of the $C_{16}OH$ surfactant used in the synthesis. Despite

decreasing the order of the calcined material, this surfactant molecule was not long enough to fully delaminate layers and prevent silanol condensation during calcination. As in Rh@IPC_C12, well-dispersed Rh NPs, with an average size of 1.71 nm were clearly visible in Rh@IPC_C16.

The $C_{22}OH$ surfactant had the strongest effect on the architecture of the final material. STEM imaging of Rh@IPC_C22 (**Fig.2c**) showed a disorganized architecture of randomly stacked layers with mesoporous voids between them. The Rh nanoparticles were uniformly distributed, which was also observed in the Rh elemental map by STEM-EDS (**Fig.S6**). The average size of the Rh nanoparticles in Rh@IPC_C22 was 1.58 nm. The relatively small and uniform size of the Rh clusters found in the final materials suggest strong interactions between the metal and the zeolite support, mainly through silanol nests, which stabilizes the Rh clusters. Although the smallest particles were produced when swelling the sample with the longest surfactant, the difference in size was nevertheless small (approximately 10%).
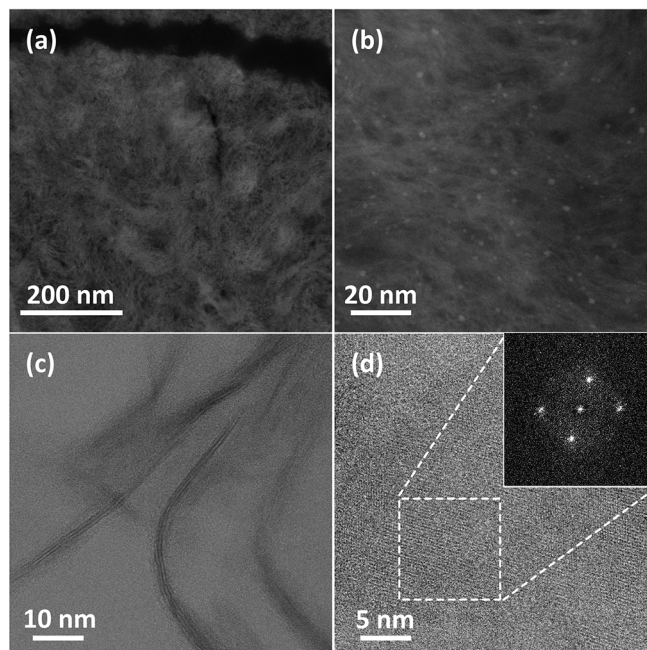

Figure 3. STEM images of cross-sections of Rh@IPC-C22 prepared by ultramicrotomy; general view of the architecture (a), stabilized Rh nanoparticles (b), delaminated IPC-1P layers at the edge of crystal domains (c), and top-view of the preserved layers with an intersected FFT pattern (d).

The Rh@IPC_C22 architecture was studied in detail by STEM using a sample prepared by ultramicrotomy STEM images of cross-sections (**Fig. 3**) showed homogenous internal crystal domains with a uniform distribution of mesopores and nanoparticles, albeit with some delaminated layers of IPC-1P at the edges of crystal domains (**Fig. 3c**). This architecture further confirms the high level of layer disorganization and even the unprecedented partial delamination of the IPC-1P layered precursor, with well-preserved and crystalline layers, clearly visible in the STEM image and in the corresponding FFT pattern of this image (**Fig. 3d**).

By in-situ heating with STEM imaging, we experimentally assessed the stability of the nanoparticles and tracked the evolution of the metal species after swelling. The results revealed changes in crystal morphology (**Fig. S8**), with a gradual disordering during heating from RT to 600 °C. Based on TG analysis (**Fig. 4f**), these changes were assigned to water desorption at an early stage of heating, followed by decomposition of the organic surfactant and metal complex.

Our detailed investigation of the materials during thermal treatment is shown in **Fig. 4**. A sample swollen at room temperature (RT) showed a relatively ordered layer arrangement, with an average d-spacing of 3.9 nm. At RT, no metal nanoparticles were identified in the sample. Consequently, rhodium remained in the form of metal complex.
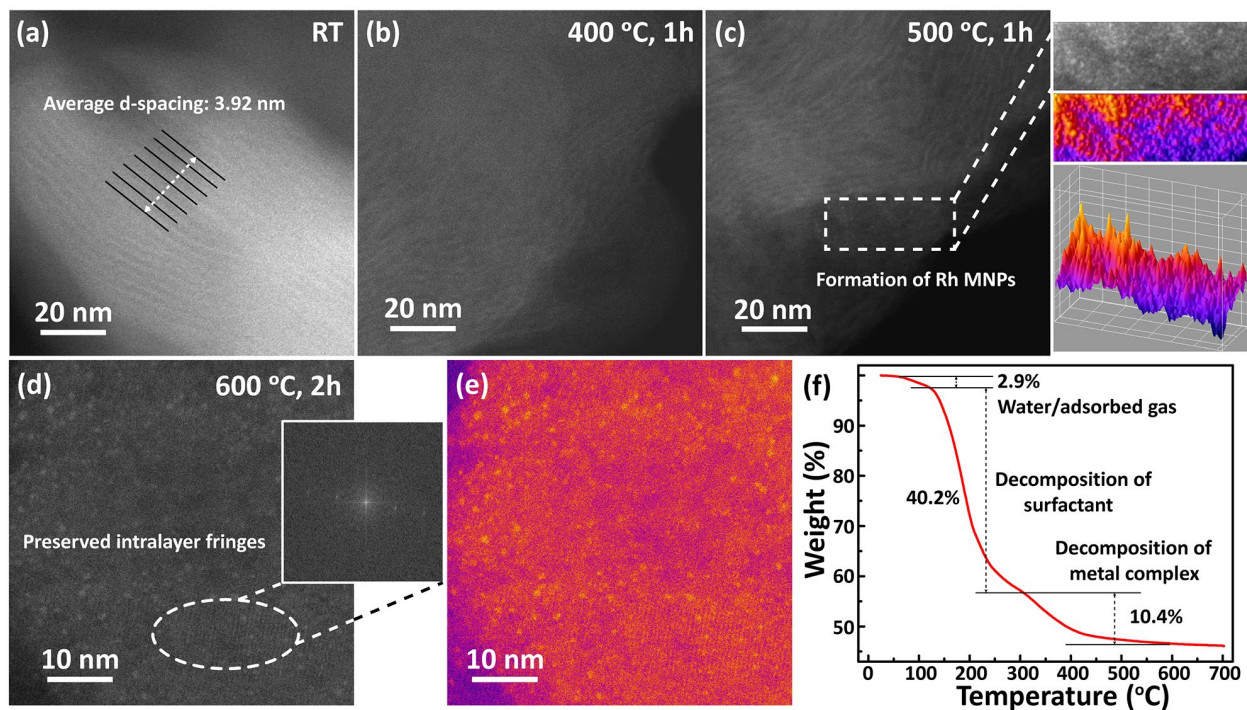
Figure 4. *In-situ* heating STEM images showing the formation of rhodium nanoparticles and the change in architecture: at room temperature (a), after heating at 400 ºC for 1 h (b), after heating at 500 ºC for 1 h, with the corresponding increase in the contrast profile (c), after heating at 600 ºC for 2 h (d), and enhanced-contrast image (e); TG plot of the Rh@IPC_C22 precursor (f).

During heating, which removed the surfactant between layers, the ordering of the swollen materials was gradually lost, with disordering becoming visible at temperatures above 400 ºC. In turn, the metal nanoparticles became visible after reaching 500 ºC. (**Fig. 4c**) Therefore, this method allows us to distinguish two structural changes, which occur at different stages of the transformation of the material upon heating: (1) the disordering of the layers and creation of mesopores, and (2) the evolution of Rh nanoparticles.

Heating to 600 ºC and maintaining the material at this temperature for 2 h showed that the resulting nanoparticles were stable and resistant to sintering at such a high temperature. In addition, the IPC-1P layers were well preserved and visible in the STEM image (**Fig. 4d)** and in its FFT pattern.
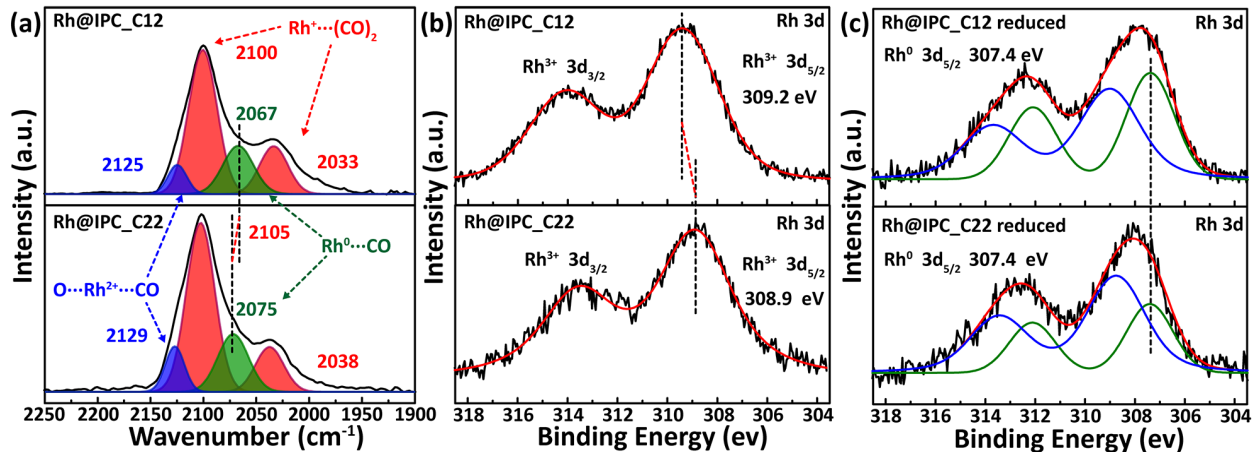

Figure 5. (a). FT-IR spectra of Rh@IPC_C22 and Rh@IPC-4_C12 after CO adsorption; (b, c) XPS spectra of the Rh@IPC materials and their corresponding materials reduced with hydrogen.

To reveal the oxidation states of Rh species intercalated in different IPC architectures and hence various chemical environments,[19] we performed X-ray photoelectron spectroscopy (XPS) (**Fig.**

5b&c). The binding energy of the rhodium species ($3d_{5/2}$) was 309.2 eV in Rh@IPC-4_C12 and 308.9 eV in Rh@IPC-C22 (**Fig. 5b**).

The open architecture of Rh@IPC-C22 allowed Rh species to interact with the silanol-rich zeolite layer surface, increasing the formation of Si-O-Rh bonds compared with Rh@IPC-C12. It shifted the spectra of Rh 3d to a lower oxidation states. Conversely, Rh@IPC-4_C12 had a much lower density of silanols because most layers were connected by Si-O-Si bridges, so the Rh-support interaction was weaker, as further confirmed by ^{29}Si SS NMR analysis (**Fig. S9**). The lower oxidation state of Rh in Rh@IPC-22 suggests that Rh binds to the support stronger in mesoporous Rh@IPC-C22 than in microporous Rh@IPC-4_C12.

This phenomenon was also confirmed by qualitative FTIR CO adsorption studies. CO adsorption resulted in the appearance of carbonyls associated with various Rh species: i) Rh^+ ions represented by $Rh^+(CO)_2$ complexes (ν_s(CO) at ~2100 cm^{-1} and ν_{as} (CO) at ~2035 cm^{-1}); and ii) metallic Rh^0 (~2070 cm^{-1}) and iii) Rh^{2+} confirmed by the presence of $O\cdots Rh^{2+}\cdots CO$ complexes (2125 cm^{-1}).[20] The angle between carbonyl groups in gem-dicarbonyl species ($Rh^+(CO)_2$) is linked with the ratio of integrated absorbance of asymmetric (~2035 cm^{-1}) and symmetric stretches (~2100 cm^{-1}).[21] In our both analyzed materials this angle is similar (~60°, **Table S2**), suggesting that the geometry of nanoparticles is analogous regardless the layer connectivity. The existence of the Rh^{2+} complex was conditioned by the presence of oxygen in the vicinity. Considering differences in the intensities (~35%) of the Rh^{2+} band, Rh@IPC_C22 had a higher population of $O\cdots Rh^{2+}\cdots CO$ species than Rh@IPC-4_C12, suggesting the influence of the local environment on the stabilization of Rh^{n+} complexes. The spectra of Rh@IPCs zeolites are presented in **Fig.5a**.

Rh^{3+} species were not detected by FTIR using CO as a probe molecule. The high charge of these ions hinders π back-donation, suggesting the low stability of the corresponding carbonyls. Rh^{3+} do not give rise to bands assigned to $Rh^{3+}\cdots CO$ complexes, that are possible to observe only under certain conditions, as previously shown in the literature. [22] Given that most rhodium occurred in the form of Rh^{3+} based on our XPS analysis, the higher number of $O\cdots Rh^{2+}\cdots CO$ complexes in Rh@IPC_C22 indicated the stabilization of Rh^{2+} species by neighboring silanol groups. Moreover, XPS is a surface-sensitive technique (around 10 nm of in-depth information), which explains the significantly higher contribution of Rh^{3+} species in this part of the sample. Further analysis of two

materials reduced in H_2 supported our assumption of stronger Rh interactions with partially delaminated layered supports with a higher concentration of surface silanols. The reduction procedure led to the appearance of the metallic form (Rh^0) of the metal species, with a binding energy of 307.4 eV, coexisting with the previously observed oxide form (**Fig.5c**). The formed Si-O-Rh makes metal species more resistant to H_2 reduction.

The amount of reduced Rh^0 varied with the Rh@IPC architecture. Therefore, in silanol-rich Rh@IPC-C22 significantly less of rhodium is reduced, suggesting that silanol nests stabilize Rh nanoparticles. To assess the stabilization of ultra-small Rh particles and the high silanol density effect on the support, we calculated the structures and migration energetics of rhodium atoms and clusters in isolated IPC-1P layers using DFT. Considering the high computational cost of nanoparticles on supports, we used the icosahedral Rh_{13} cluster as a model for the three-dimensional, pseudo-spherical particles observed by STEM. This cluster was large enough to occupy all four silanol groups of a single quadruplet but not to trigger interactions between clusters in adjacent quadruplets.

Our DFT calculations also showed that initially reduced Rh_1 and Rh_{13} strongly bind to the hydroxylated surface (around -2 eV), indicating effective immobilization by silanol nests. For Rh_{13}, all four silanol oxygen atoms of one silanol nest can be simultaneously bound to Rh, which lies at the center of the quadruple (**Fig. 6**). For the experimentally observed particles, with a mean diameter < 1.9 nm, silanol groups from adjacent silanol nests will unlikely have a significant contribution; however, this contribution cannot be ruled out for larger particles.

We then considered an alternative model for the cluster in which successive silanol hydrogen atoms are transferred to the rhodium particle, leading to $Rh_{13}[H_x]@IPC\text{-}1P[H_{4-x}]$ (x = 0-4). The transfer of hydrogens is significantly exoenergetic, resulting in a maximum binding energy of approximately -5 eV for $Rh_{13}[H_4]@IPC\text{-}1P$ (**Table S3**). In this configuration, the Rh_{13} cluster obtains a charge of +3.25 (formal charge + 4). This charge separation mechanism in which a positively charged metal sub-hydride is electrostatically pinned to the negatively charged surface most likely enhances the stability of the particle against sintering. Yet, despite the strong binding of the atoms and clusters to the layer, particle growth should be thermodynamically favorable given the high cohesive energy of rhodium (5.75 eV/atom for bulk Rh).
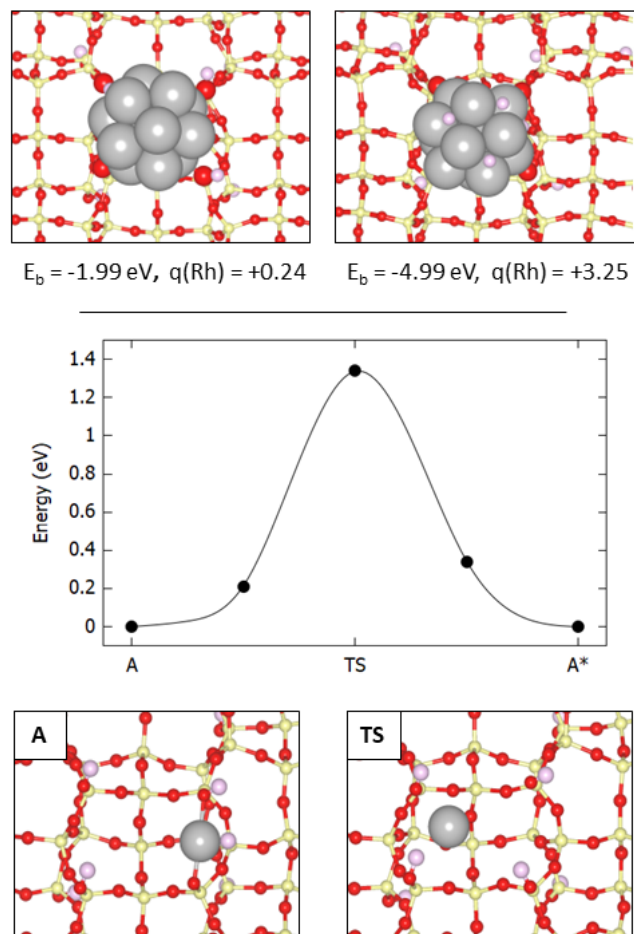
$E_b = -1.99\ eV,\ q(Rh) = +0.24$ $E_b = -4.99\ eV,\ q(Rh) = +3.25$

Figure 6. Calculated Rh_x configurations on IPC-1P layer; top: structures of Rh_{13} clusters atop the silanol quadruplet in $Rh_{13}@IPC-1P[H_4]$ (left) and $Rh_{13}[H_4]@IPC-1P$ configurations (right); bottom: reaction profile of direct Rh_1 migration across a silanol quadruplet; Rh, Si, O and H are represented in silver, yellow, red and pink, respectively.

Considering the above, we analyzed the role of the hydroxylated surface in hindering Rh migration, and thus sintering, via kinetic control. We calculated a pathway assuming an Ostwald ripening mechanism in which Rh_1 moves across the IPC-1P surface. This route involves direct, Rh_1 migration between global minimum O-Rh[H]-O sites (**Table S4, Fig S10**) across the silanol quadruplet and proceeds via a single transition state, with a reasonably high activation energy of 1.34 eV (**Fig. 6**). By comparison, the migration barrier for Rh_1 across the silanol-free model surface of silicatene, which consists of a pristine bilayer of Si-O bonds connected in a hexagonal pattern, is lower than 0.1 eV (**Fig. S11**). An alternative migration pathway involving hops between adjacent

silanol groups within a quadruplet also exhibits a barrier of over 1 eV and proceeds via intermediate structures, which are significantly endoenergetic (**Fig. S12**).

In conclusion, the presence of silanols grouped as quadruplets severely hinders the migration of Rh atoms and likely slows Ostwald ripening processes, even under conditions that energetically favor sintering, in line with our in-situ heating STEM imaging and stability tracking results (**Fig. 4** and **S8**).

To assess the effect of the architecture of our materials on product shape selectivity and Rh NP stability under reaction conditions, we used benzonitrile (BN) hydrogenation as a model reaction. The results presented in **Fig. S13** suggest that the novel mesoporous Rh@IPC_C22 is an active hydrogenation catalyst with improved mass-transfer properties thanks to its open structure. In particular, the STEM images of the spent catalyst and particle size distribution analysis (**Fig. S14 and S15)** showed no significant sintering of Rh nanoparticles, (which increased by only 10% on average, confirming the high stability of these metal species under reaction conditions. In short, metal aggregation is prevented in all three synthesized Rh@IPC materials, regardless of the presence of micropores (i.e., in Rh@IPC-4_C12).

The smallest Rh species (averaging 1.58 nm) were found in the material swollen with longest surfactant, that is, Rh@IPC_C22 (without micropores), contradicting previous reports of metal intercalation and spatial confinement in **MWW** zeolite [9]. This finding supports our hypothesis that stabilization is determined by the local environment and features of the layers, such as silanol arrangement (e.g., in quadruplets) and density, which differ between **MWW** and IPC layers as discussed in detailed in SI). In contrast to MCM-22P, IPC-1P zeolite layers showed decreased ordering with the increase in surfactant molecule length. In Rh@IPC_C22, most IPC-1P layers were delaminated and separated, thus lacking microporosity. Although the layers were not orderly connected, this novel material had an excellent distribution of ultra-small metal species. Combined, these results highlight that Rh stabilization in IPC-1P layers is determined by metal-silanol interactions, not by spatial confinement.

Conclusions

We prepared a novel, Rh-doped mesoporous material based on zeolitic layers. Rh nanoparticles encapsulated in this unprecedented material were ultra-small, well-distributed, and sintering-

resistant. Swelling and simultaneously functionalizing the UTL-derived layered zeolite precursor IPC-1P with Rh, followed by calcination, produces Rh@IPC-4_C12, Rh@IPC_C16, and Rh@IPC_C22 materials. The architecture of Rh@IPC materials can be adjusted by controlling the surfactant length, with the longest surfactant ($C_{22}OH$) producing mesoporous Rh@IPC_C22 without micropores in an unprecedented modification of an IPC-1P layered zeolite precursor. Ultra-small Rh particles that are resistant to sintering can also be selectively trapped, with STEM imaging showing the location and size distribution of Rh species in the final materials and in-situ heating STEM imaging highlighting architectural changes in the materials and the formation of Rh nanoparticles. The layer arrangement changes independently of nanoparticle evolution because the swelling agent is removed and the architecture is transformed below 400 ºC, whereas the nanoparticles are formed at higher temperature. The nanoparticles are stable at 600 ºC, showing no clear change in size after 2h. They are also stable under conditions suitable for catalytic hydrogenation of benzyl nitrile. In particular, the Rh@IPC_C22 catalyst is more selective (68%) to bulky products than the commercial Rh/C catalyst. As shown by in-situ heating STEM imaging and XPS experiments and supported by DFT calculations, the surface silanols of IPC-1P layers stabilize Rh nanoparticles. As such, IPC-1P is a benchmark precursor for decoupling metal confinement from silanol pinning effects. The resulting lack of intralayer micropores allows us to investigate metal-silanol interactions exclusively dependent on the local environment (layer arrangement and silanol density), without additional steric hindrance effects. In summary, novel materials with tunable porosity can be prepared from zeolite layered precursor whose surface silanols are stabilize ultra-small Rh nanoparticles, producing an active and sustainable hydrogenation catalyst selective to bulky molecules.

Note

The authors declare no competing financial interest.

Experimental Section

Synthesis of IPC-1P and IPC-4: To prepare IPC-1P, calcined **UTL** zeolites (synthesis procedure is described in SI) were hydrolyzed in 1M acetic acid as previously reported.[10a, 23] Typically, calcined **UTL** zeolite was hydrolyzed and stirred in 1M acetic acid at 85 $^{\circ}$C overnight (16 hours). The weight/volume ratio of calcined **UTL** zeolite to HAc solution was 1 g/1000 ml. The product was isolated by filtration, washed with an excess of deionized water twice, and dried at 65 $^{\circ}$C overnight. IPC-4 was synthesized as previously reported.[10c] Briefly, 0.3 g of IPC-1P obtained in the last step was mixed with 20 g octylamine, refluxed at 70 $^{\circ}$C for 2 hours and then stirred at room temperature overnight. The solid was isolated by centrifugation and then washed and dried at 65 $^{\circ}$C, and then calcined at 550 $^{\circ}$C for 2 hours.

Synthesis of Rh@IPC_C22, Rh@IPC_C16 and Rh@IPC-4_C12: Docosyltrimethylammonium bromide (C_{22}Br), cetyltrimethylammonium bromide (C_{16}Br) and dodecyltrimethylammonium bromide (C_{12}Br) were dispersed in 25 wt% surfactant solutions and then ion-exchanged to the OH$^-$ form (noted as C_{12}OH, C_{16}OH, and C_{22}OH) using an Ambersep 900 OH resin with a weight ratio of 70 g resin/ 100 g solution. The rhodium-incorporated IPC zeolite material Rh@IPC-4_C12 was prepared by dissolving of the required amount of rhodium(II) acetate dimer in 5 ml EtOH, and treated with ultrasound until homogeneous. Then, 1 ml of ethylenediamine was added to the metal precursor, subsequently mixing 0.2 g IPC-1P, 10g 25 wt% C_{12}OH surfactant solution, 10 g deionized water, and the Rh ethanol solution and stirring vigorously overnight at room temperature. The product was separated by centrifugation and washed with distilled water 5 times. The solids were dried at 65 $^{\circ}$C overnight and then calcined in air at 550 $^{\circ}$C for 6 h to remove the organics

with a temperature ramp of 1 °C min^{-1}. The final materials were denoted as Rh@IPC-4_C12. Rh@IPC_C16 and Rh@IPC_C22 were synthesized using similar the procedures, except for the use of different surfactant molecules during the swelling step: $C_{16}OH$, and $C_{22}OH$, denoting the final materials as Rh@IPC_C16 and Rh@IPC_C22, respectively.

Further experimental details are included in Supporting Information.

References

[1] a) L. Liu, A. Corma, *Chem. Rev.* **2018**, *118*, 4981-5079; b) C. Y. Dong, Y. L. Li, D. Y. Cheng, M. T. Zhang, J. J. Liu, Y. G. Wang, D. Q. Xiao, D. Ma, *ACS Catal.* **2020**, *10*, 11011-11045; c) B. C. Gates, *Chem. Rev.* **1995**, *95*, 511-522.

[2] a) L. Wang, L. Wang, X. Meng, F. S. Xiao, *Adv. Mater.* **2019**, *31*, e1901905; b) B. C. Gates, M. Flytzani-Stephanopoulos, D. A. Dixon, A. Katz, *Catal. Sci. Technol.* **2017**, *7*, 4259-4275; c) L. C. Liu, A. Corma, *Nat. Rev. Mater.* **2020**, *6,* 244–263.

[3] a) N. Wang, Q. Sun, J. Yu, *Adv. Mater.* **2019**, *31*, e1803966; b) S. M. Wu, X. Y. Yang, C. Janiak, *Angew. Chem. Int. Ed.* **2019**, *58*, 12340-12354.

[4] a) Y. Li, J. H. Yu, *Chem. Rev.* **2014**, *114*, 7268-7316; b) Y. Li, J. H. Yu, *Nat. Rev. Mater.* **2021**; c) M. Babucci, A. Guntida, B. C. Gates, *Chem. Rev.* **2020**, *120*, 11956-11985.

[5] a) D. Farrusseng, A. Tuel, *New J. Chem.* **2016**, *40*, 3933-3949; b) N. Kosinov, C. Liu, E. J. M. Hensen, E. A. Pidko, *Chem. Mater.* **2018**, *30*, 3177-3198; c) Y. Chai, W. Dai, G. Wu, N. Guan, L. Li, *Acc. Chem. Res.* **2021**, *54*, 2894-2904.

[6] a) M. Choi, Z. Wu, E. Iglesia, *J. Am. Chem. Soc.* **2010**, *132*, 9129-9137; b) S. Goel, Z. Wu, S. I. Zones, E. Iglesia, *J. Am. Chem. Soc.* **2012**, *134*, 17688-17695; c) N. Wang, Q. Sun, R. Bai, X. Li, G. Guo, J. Yu, *J. Am. Chem. Soc.* **2016**, *138*, 7484-7487; d) T. L. Cui, W. Y. Ke, W. B. Zhang, H. H. Wang, X. H. Li, J. S. Chen, *Angew. Chem. Int. Ed.* **2016**, *55*, 9178-9182; e) C. Wang, L. Wang, J. Zhang, H. Wang, J. P. Lewis, F. S. Xiao, *J. Am. Chem. Soc.* **2016**, *138*, 7880-7883; f) J. Zhang, L. Wang, B. S. Zhang, H. S. Zhao, U. Kolb, Y. H. Zhu, L. M. Liu, Y. Han, G. X. Wang, C. T. Wang, D. S. Su, B. C. Gates, F. S. Xiao, *Nat. Catal.* **2018**, *1*, 540-546; g) S. Molitorisová, Y. Zhang, M. Kubů, A. Li, Z. Tošner, M. Shamzhy, *Catal. Today* **2021**; h) R. Ryoo, J. Kim, C. Jo, S. W. Han, J. C. Kim, H. Park, J. Han, H. S. Shin, J. W. Shin, *Nature* **2020**, *585*, 221-224; i) N. Wang, Q. Sun, T. Zhang, A. Mayoral, L. Li, X. Zhou, J. Xu, P. Zhang, J. Yu, *J. Am. Chem. Soc.* **2021**, *143*, 6905-6914; j) M. Numan, E. Eom, A. Li, M. Mazur, H. W. Cha, H. C. Ham, C. Jo, S.-E. Park, *ACS Catal.* **2021**, *11*, 9221-9232.

[7] H. Wang, L. Wang, F. S. Xiao, *ACS Cent. Sci.* **2020**, *6*, 1685-1697.

[8] a) L. Liu, U. Diaz, R. Arenal, G. Agostini, P. Concepción, A. Corma, *Nat. Mater.* **2017**, *16*, 132-138; b) L. Liu, R. Arenal, D. M. Meira, A. Corma, *Chem. Commun.* **2019**, *55*, 1607-1610.

[9]   Y. Y. Zhang, M. Kubu, M. Mazur, J. Cejka, *Catal. Today* **2019**, *324*, 135-143.

[10] a) W. J. Roth, O. V. Shvets, M. Shamzhy, P. Chlubná, M. Kubů, P. Nachtigall, J. Čejka, *J. Am. Chem. Soc.* **2011**, *133*, 6130-6133; b) P. Chlubná, W. J. Roth, H. F. Greer, W. Zhou, O. Shvets, A. t. Zukal, J. i. Čejka, R. E. Morris, *Chem. Mater.* **2013**, *25*, 542-547; c) W. J. Roth, P. Nachtigall, R. E. Morris, P. S. Wheatley, V. R. Seymour, S. E. Ashbrook, P. Chlubna, L. Grajciar, M. Polozij, A. Zukal, O. Shvets, J. Cejka, *Nat. Chem.* **2013**, *5*, 628-633.

[11] a) M. T. Jin, O. Vesely, C. J. Heard, M. Kubu, P. Nachtigall, J. Cejka, L. Grajciar, *J. Phys. Chem. C* **2021**, *125*, 23744-23757; b) Z.-P. Hu, J. Han, Y. Wei, Z. Liu, *ACS Catal.* **2022**, 5060-5076.

[12] P. Eliasova, M. Opanasenko, P. S. Wheatley, M. Shamzhy, M. Mazur, P. Nachtigall, W. J. Roth, R. E. Morris, J. Cejka, *Chem. Soc. Rev.* **2015**, *44*, 7177-7206.

[13] J. L. Paillaud, B. Harbuzaru, J. Patarin, N. Bats, *Science* **2004**, *304*, 990-992.

[14] a)T. Blasco, A. Corma, M. J. Diaz-Cabanas, F. Rey, J. A. Vidal-Moya, C. M. Zicovich-Wilson,   *J. Phys. Chem. B* **2002**, *106*, 2634-2642; b) G. Sastre, J. A. Vidal-Moya, T. Blasco, J. Rius, J. L. Jorda, M. T. Navarro, F. Rey, A. Corma, *Angew. Chem. Int. Ed.* **2002**, *41*, 4722-4726.

[15] Y. Y. Zhang, M. Kubu, M. Mazur, J. Cejka, *Microporous Mesoporous Mater.* **2019**, *279*, 364-370.

[16] a) D. Hou, L. Grajciar, P. Nachtigall, C. J. Heard, *ACS Catal.* **2020**, *10*, 11057-11068; b) D. Hou, C. J. Heard, *Catal. Sci. Technol.* **2022**; c) J. Kim, S. W. Han, J.-C. Kim, R. Ryoo, *ACS Catal.* **2018**, *8*, 10545-10554; d) S. V. Konnov, F. Dubray, E. B. Clatworthy, C. Kouvatas, J. P. Gilson, J. P. Dath, D. Minoux, C. Aquino, V. Valtchev, S. Moldovan, S. Koneti, N. Nesterenko, S. Mintova, *Angew. Chem. Int. Ed.* **2020**, *59*, 19553-19560. e) F. Dubray, S. Moldovan, C. Kouvatas, J. Grand, C. Aquino, N. Barrier, J.-P. Gilson, N. Nesterenko, D. Minoux, S. Mintova, *J. Am. Chem. Soc.* **2019**, *141*, 8689-8693.

[17] L. Liu, M. Lopez-Haro, J. A. Perez-Omil, M. Boronat, J. J. Calvino, A. Corma, *Nat. Commun.* **2022**, *13*, 821.

[18] J. Y. Zhu, F. M. Li, L. Yao, C. C. Han, S. N. Li, J. H. Zeng, J. X. Jiang, J. M. Lee, Y. Chen, *CrystEngComm.* **2017**, *19*, 2946-2952.

[19] a) C. Force, E. Roman, J. M. Guil, J. Sanz, *Langmuir* **2007**, *23*, 4569-4574. b) Y. V. Larichev, O. V. Netskina, O. V. Komova, V. I. Simagina, *Int. J. Hydrog. Energy* **2010**, *35*, 6501-6507; c) M. Hussain, D. Fino, N. Russo, *J. Hazard. Mater.* **2012**, *211-212*, 255-265.

[20] a) R. Lang, T. Li, D. Matsumura, S. Miao, Y. Ren, Y.-T. Cui, Y. Tan, B. Qiao, L. Li, A. Wang, X. Wang, T. Zhang, *Angew. Chem. Int. Ed.* **2016**, *55*, 16054-16058. b) K. I. Hadjiivanov, G. N. Vayssilov, *Adv. Catal.* **2002**, *47*, 307-511.

[21] J. T. Yates, T. M. Duncan, S. D. Worley, R. W. Vaughan, *J. Chem. Phys.* **1979**, *70*, 1219-1224.

[22] a) S. Trautmann, M. Baerns, *J. Catal.* **1994**, *150*, 335-344. c) F. Basile, I. Bersani, P. Del Gallo, S. Fiorilli, G. Fornasari, D. Gary, R. Mortera, B. Onida, A. Vaccari, *Int. J. Spectrosc.* **2011**, *2011*, 1-8.

[23] M. Mazur, P. Chlubna-Eliasova, W. J. Roth, J. Cejka, *Catal. Today* **2014**, *227*, 37-44